Lasers in Manufacturing and Materials Processing (2024) 11:154–178
https://doi.org/10.1007/s40516-023-00244-3

RESEARCH

Temporal and Spatial Beam Shaping in LPBF for Fine and Porous Ti-Alloy Structures for Regenerative Fuel Cell Applications

Salomé Sanchez[1] · Ahmad Zafari[1] · Leonardo Caprio[2] · Ali Gökhan Demir[2] · Davoud Jafari[1]

Accepted: 28 December 2023 / Published online: 1 February 2024

Abstract

Laser Powder Bed Fusion (LPBF) presents itself as a potential method to produce thin porous structures, which have numerous applications in the medical and energy industries, due to its in-process pore formation capabilities. Particularly, regenerative fuel cells, which are capable of both producing and storing energy through the use of hydrogen-based electrochemical fuel cell and electrolysers, respectively, can benefit from the LPBF-induced porosity for it porous layer components in the electrode. Numerous studies have reported that process parameters, such as laser power, scan speed and hatch spacing, are key factors affecting the formation of pores in LPBF material due to their control over the energy density and melt pool formation during the build. Contemporary fibre lasers offer novel temporal and spatial beam shaping capabilities. Temporal laser control means that the laser can use pulsed wave (PW) or single point exposure (SPE), and spatial beam shaping refers to variations in the intensity distribution of the laser, which can be modulated from Gaussian to ring shape via the use of multi-core fibers. These have seldom been studied in combination with LPBF. Therefore, the aim of this study was to utilise temporal and spatial beam shaping in LPBF to produce thin porous structures. To do this, PW and SPE laser temporal strategies were utilised and the duty cycle (which relates the on and off time of the laser) was varied between 50% and 100%. Beam shape indexes 0 (Gaussian), 3 and 6 (ring) were also investigated alongside more standard LPBF process parameters such as laser power and scan speed to manufacture thin porous walls, as well as fine struts. The thinnest wall obtained was 130 µm thick, while the smallest strut had a diameter of 168 µm. The duty cycle had a clear effect on the porosity of thin walls, where a duty cycle of 50% produced the highest number of porous walls and had the highest porosity due to its ability to control the intensity of the energy density during the LPBF process. The different beam shape indexes corresponded to different spatial distribution of the power density, and

✉ Davoud Jafari
davoud.jafari@utwente.nl

Extended author information available on the last page of the article

hence, modifying the temperature distribution in the meltpool during the laser material interaction. Beam shape index 6 (corresponding to a ring mode with lower peak irradiance) created more porous specimens and smaller meltpool sizes, with respect to its beam size. Overall, this study showed that temporal and spatial control of the beam (through duty cycle and beam shape index) are powerful tools which can control the distribution and intensity of the energy density during the LPBF process to produce thin porous structures for energy applications.

Keywords Laser Powder Bed Fusion · Beam shape index · Duty cycle · Ti-6Al-4V · Thin walls · Porous structures · Regenerative fuel cells

Introduction

Climate change, combined with increasing energy demands, requires investments in energy conversion and storage systems, such as regenerative fuel cells, batteries, and supercapacitors. Among other benefits, these systems have the potential to remedy to the intermittent and variable energy generation issues present in renewable energy production. In the case of regenerative fuel cells, when there is a high generation of electricity but low demand, the regenerative fuel cell can convert electricity to hydrogen, as a form of energy storage, and when the production of electricity is too low, the fuel cell can take the stored hydrogen and convert it back into electricity. To optimise their performance, these systems require advanced materials, such as electrodes and metallic gas diffusion layers, with high conductivity, tailored porous structures and surface chemistry [1]. These structures are usually thin (< 400 µm thickness) [2] and require multiscale porosity with pore size ranging from 10 to 100 µm to enhance electrode efficiency and life [3]. Current materials for these electrodes include Ni foam and Ti felt, which offer a thin porous layer. However, the amount and location of porosity cannot be controlled in these materials. In this paper, we aim to tackle the challenges mentioned above, specifically, to control pore size, pore distribution and the thickness of porous structures, that potentially will pave the way for an improvement in the performance of electrochemical technologies. To achieve these goals, Laser Powder Bed Fusion (LPBF), a metal additive manufacturing process, is capable of fabricating complex designs, such as lattice structures, which are composed of a repetition of unit cells with various volume fraction porosity. These structures are capable of defining the pore size and distribution in structures. However, limits in LPBF feature resolution (~ 100 µm) [4] result in pores of ~ 100–200 µm diameter, which are too large for these applications. Another possibility is to induce pore formation during the LPBF process by manipulating process parameters, such as laser power, scan speed and scan strategy. For Ti-6Al-4V, at a laser power of 160 W, fully dense specimens are obtained with scan speeds between 600 mm/s and 1600 mm/s [5]. Depending on the laser power and scan speed combination employed, both fully dense and porous parts can be obtained. Studies have shown that keyhole porosity occurs when utilising high laser powers (between 200 and 500 W) [6] and low scan speeds, which creates a vapour cavity in the meltpool to produce rounded pores

[7]. Inversely, lack-of-fusion porosity is mostly present at low laser powers and high scan speeds, creating inadequate melting between tracks and layers [8]. In general, a review by Shipley et al. on the optimisation of Ti-6Al-4V process parameters, showed that more porosity is present when using laser powers below 100 W, regardless of the scan speed [5]. There is therefore an opportunity to utilise the LPBF in-process pore formation to fabricate thin porous structures. In a previous study, Abele et al. obtained LPBF 316L stainless steel walls with a maximum porosity of 17.5% and a minimum thickness of 125 µm by varying laser power, scan speed, and hatch distance [9], while other studies have obtained thin walls of 140 µm [10] and 100 µm [11] for stainless steel 904L and stainless steel 316L, respectively. Additionally, Xie et al. revealed that 17% of pores in a 1 mm thick 316 stainless steel wall had a diameter of 14 µm or less [12]. The results from these initial studies are promising as they show that thin walls and high porosity can be achieved with LPBF. However, advancing the LPBF process further is necessary for developing thin porous structures with tailored microstructures, controlled porosity, and precisely engineered surface morphology.

Contemporary laser sources provide several options to generate thin porous structures during the LPBF process. In particular, temporal and spatial control of the beam profile can provide the means to design and generate both deterministic and stochastic features with variable dimensions. The use of Pulsed Wave (PW) and Continuous Wave (CW) emissions has been the matter of debate over the last decade concerning the feature resolution and productivity concerns in LPBF [13]. It has been shown that PW generated via the fast modulation of free running fibre lasers can provide a fine control of the heat input and hence improve the process and feature resolution [14]. The use of PW emission with µs-long pulses has also been shown to be effective for generating interconnected stochastic pores [15]. The laser source is pulsated as it moves along the scan path, generating partial fusion and fusion separation between the tracks and along the layers. The structure is composed of the conventionally named lack-of-fusion type of porosity. If the process parameters can be opportunely controlled, one can achieve interconnected pores useful for wicking and storage applications. Similarly, the lasers can be used to emit only a limited amount of energy on a single point rather than scanning over vectors and areas. This so-called Single Point Exposure (SPE) can provide the means to reduce cylindrical strut dimensions close to the size of the laser beam (50–100 µm) and comparable to powder particle size (10–50 µm) [16]. The use of such strategy can be exploited in a layer-by-layer fashion for deterministically porous structured by means of producing micro lattices [17]. In this current study, SPE arises as a promising method to obtain fine struts, which can lead to the creation of high resolution lattice structures for thin porous structures.

A more recent novelty of contemporary fibre lasers is the use of in-source beam shaping technology. Multi-core fibre lasers can emit beam profiles from the conventional Gaussian towards the novel ring shapes [18]. Beam shaping has been shown to affect the temperature distribution in the meltpool, which in turn can influence feature resolution and porosity [19]. While their use in LPBF has been shown in single track studies to bulk deposits [20], their use in porous thin layers is yet to be analysed. The combined flexibility of the contemporary laser sources requires open hardware and a careful study to correct parametric definition.

In this context, this paper aims to explore the potential of LPBF for the fabrication of thin (~ 100–200 µm) Ti-6Al-4V porous structures. Ti-6Al-4V is widely used in various industries, such as marine, aerospace and biomedicine, as it possesses a favourable combination of strength and ductility, as well as great corrosion resistance. The poor machinability and high cost of Ti-6AL-4V also make LPBF a viable processing option. This study utilises spatial and temporal beam shaping in LPBF to discuss the effect of various process parameters and highlight the challenges and opportunities associated with the proposed approach for the manufacturing of thin porous structures. By gaining a deeper understanding of LPBF's capabilities and limitations, researchers and engineers can unlock new possibilities in fields such as biomedical engineering, filtration, and energy conversion and storage systems, such as regenerative fuel cells, in the manufacture of thin porous layers.

Experimental Methods

The aim of this study is to understand PW, SPE and spatial beam shaping effects on LPBF fabricated fine struts and porous thin walls. The thin wall geometry was selected to imitate the geometry of a regenerative fuel cell electrode and minimise thickness, whereas the fine struts were studied with the aim of making fine lattice structures, which adequately control the volume fraction density and location of pores. First, thin walls and struts were printed using various process parameters. Then, the thickness and porosity of the thin walls were characterised, as well as the diameter of the struts.

Laser Powder Bed Fusion

A TEKNA (Mâcon, France) Ti-6Al-4V powder, with a mean particle diameter of 38.8 µm, particle size distribution of 15–45 µm (measured according to ASTM B822 [21]), and an elemental composition reported in Table 1, was used.

Table 1 Elemental composition of TEKNA Ti-6Al-4 V powder

Element	Concentration (wt%)
Al	6.50
Fe	0.20
V	4.01
Y	< 0.001
C	0.008
H	0.002
N	0.008
O	0.11
Other elements, each	< 0.10
Other elements, total	< 0.40
Ti	Balance

An industrial, research grade 3D-NT LLA150 (3D New Technologies S.r.l, Torino, Italy) LPBF machine was used throughout the experimental work to fabricate the specimens. The system was equipped with a nLIGHT, AFX1000 (Vancouver, WA, USA) laser source with in-source beam shaping capability. The laser could change the beam profile with pre-defined beam shape indexes (BS) from the conventional Gaussian towards a ring profile by redistributing the emission power from the inner core towards a second outer core (i.e. ring) of the transport fiber. The inner core of the transport fiber corresponded to 14 µm whilst the outer core of the transport fiber was 40 µm. The emission wavelength of the laser beam corresponded to 1070 nm, with a maximum emission power of 600 W in the inner core and 1200 W in the outer core. The laser beam from the multi-core transport fiber was collimated by means of a 60 mm focal length lens, enlarged with a 1.25 X beam expander and focused via an F-Theta lens with 254 mm focal length The LPBF machine was controlled using a tailor made software by DMC (Vilnius, Lithuania). The software allowed to change the emission profile between PW and CW, to manufacture thin walls, as well as the use of SPE to fabricate the thin struts. The laser source was coupled to a scanner head (MiniScan III, Raylase, Weßling, Germany) producing a focused spot size of 49 µm for the Gaussian profile (BS0) whilst the minimum waist diameter for the ring (BS6) was measured at 144 µm. The beam divergence declared from the producer corresponded to 0.48 mm•mrad for the BS0 and 2.1 mm•mrad for BS6. The beam waist diameter was measured by exposing a CCD camera (Gentec Beamage Series USB 3.0, Quebec City, Canada) to an attenuated beam. Further details regarding the optical propagation are reported in a previous publication [19]. Table 2 reports the main characteristics of the 3 beam shapes investigated.

BS3 is a mixed form composed of a central peak and a ring around it. The irradiance of the different beam shape indexes (at a constant level of power P = 200 W) are illustrated in Fig. 1. Observing the different power distribution it is possible to denote how the peak emission level decreases from BS0 to BS6 whilst the overall emission power is maintained constant.

Throughout the build process, 99.998% purity Ar was cycled over the powder bed maintaining the oxygen content below 3000 ppm. A Ti-6Al-4V baseplate was used during the build.

Thin Walls

The thin walls were designed as single-laser tracks of 15 mm in length over a height of 10 mm. Various process parameters were investigated in order to manufacture thin and porous walls. PW was used as it has been previously shown to result in

Table 2 Main characteristics of the beam shapes used in the experiments (for more information, see [22])

Beam shape index (BS)	BS0	BS3	BS6
Power ratio (ring/core)	0/100	50/50	90/10
Closest Laguerre-Gaussian TEM	TEM00	TEM10	TEM01*
Beam size, d_0 (µm)	49	112	144

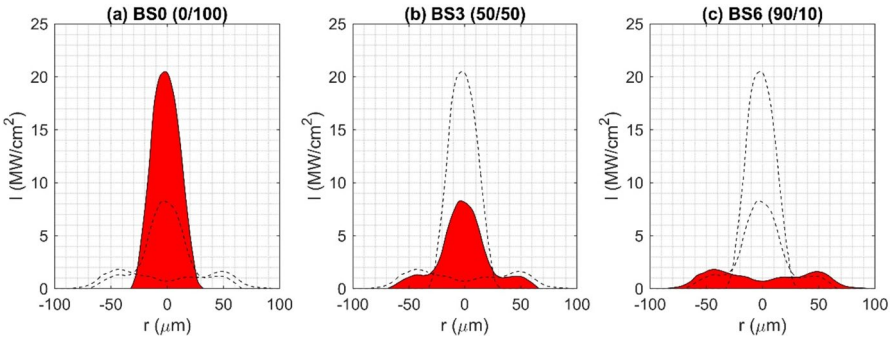

Fig. 1 Measured irradiance profiles for the different beam shapes (**a**) BS0 (0/100), (**b**) BS3 (50/50) and (**c**) BS6 (90/10) at P = 200 W

higher feature resolution of LPBF parts as compared to CW [23]. PW systems have additional process parameters, such as duty cycle (δ), which relates the time on (t_{on}) and time off (t_{off}) of the laser:

$$\delta = \frac{t_{on}}{t_{on} + t_{off}}$$

The duty cycle was varied in order to compare various PW cycles. The laser power and scan speed were also varied as they have been previously shown to have significant effects on the melt pool size and porosity of LPBF parts [5]. Finally, the beam shape index was also varied to investigate its effect on the thickness and porosity of the LPBF parts. The aim of this study was to verify the consolidation behaviour, without necessarily obtaining elevated levels of part density. Table 3 gives an overview of both the fixed and varied process parameters to manufacture the thin walls using PW. The beam shape indexes were selected to see the effects of different intensity profiles, towards a possibly more homogenous intensity distribution. The broad range of duty cycles were investigated to understand how various cooling phases would affect consolidation. Laser power and scan speed parameters were

Table 3 Overview of the fixed and variable LPBF process parameters used for fabricating thin walls

LPBF process parameters	Values
Variable parameters	
Beam shape index	0; 3; 6
Duty cycle (%)	50; 75; 100
Laser Power (W)	100; 150; 200
Scanning speed (mm/s)	500; 1000; 1500
Fixed parameters	
Layer thickness (μm)	30
Focal point (mm)	0
Time off (μs)	20

varied, starting with parameters for fully-dense Ti-6Al-4 V, towards parameters to obtain porous structures. The focal position, also known as the focal point, was kept at 0 mm, i.e. on the nominal surface.

Fine Struts

The struts were fabricated using SPE to obtain the smallest diameter possible over a height of 10 mm. For SPE, there is only a single laser pulse, and hence, there is no set time off. Therefore, time on, laser power and beam shape index were varied to manufacture the thin struts with SPE and an overview of the process parameters employed in the experimental design is given in Table 4.

Both the thin walls and the struts were printed at the same time, on the same build plate. The specimens were not stress relieved or heat treated after the build.

Characterisation

After printing, the thin walls and the struts were characterised using imaging techniques to obtain information regarding the wall thickness, strut diameter and porosity.

Wall Thickness and Strut Diameter Measurements

The wall thickness and the diameter of the struts were measured by using a Quickvision, PRO system (Mitutoyo, Kawasaki, Kanagawa, Japan). The thin walls and struts were kept attached to the build plate and observed from the top (i.e. perpendicular to the build direction (BD), as illustrated in Fig. 2) in order to get images and measurements of the wall thickness and diameters. A magnification of 2500 × and 5000 × was used for the thin walls and the struts, respectively. For measuring the wall thickness, 5 measurements were taken along the thin wall (Fig. 2a), while 2 diameter measurements were taken for the fine struts (Fig. 2b). Powder particles attached to the sides of the thin walls and around the struts were counted as part of the thickness and diameter measurements. For the fine struts, the difference in the 2 diameters was also used to calculate the aspect ratio of the cylindrical struts. The repeated

Table 4 Overview of the fixed and variable LPBF process parameters used for fabricating fine struts

LPBF process parameters	Values
Variable parameters	
Beam shape index	0; 3; 6
Time on (μs)	50; 100; 200; 400; 800
Laser Power (W)	100; 150; 200
Fixed parameters	
Layer thickness (μm)	30
Number of pulses	1
Focal point (mm)	0

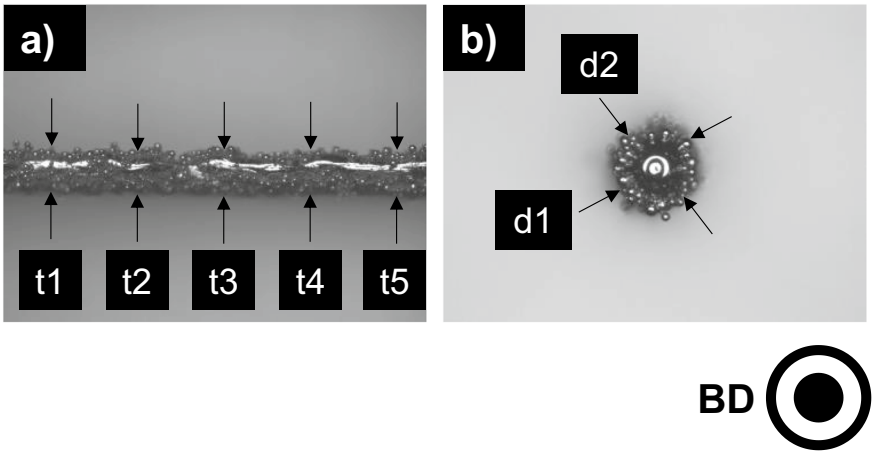

Fig. 2 Illustration of how the measurements for the (**a**) thin walls, where 5 thickness measurements (t1 to t5) were taken along the length of the wall; (**b**) fine struts, where 2 diameter values (d1 and d2) were taken for each strut. For both the thin walls and the fine struts, powder particles attached to the surfaces were taken into account in the measurements

measurements were averaged in both cases. The standard error was calculated from the variation of the repeats to produce error bars in subsequent graphs.

Porosity Measurements

Following the thickness measurements, the struts and the thin walls were removed from the build plate and were placed in an ultrasonic bath of ethanol solution for 5 min to remove loose powders. Thereafter, porosity measurements began.

The Archimedes method was not utilised to calculate the density of the thin walls, as the dimensions and surface roughness of the specimens resulted in the formation of water bubbles, which stayed on the surface of the specimens when weighed in water. Additionally, numerous thin walls did not submerge in the water, and would instead float on the surface, making measurements difficult. Therefore, imaging techniques were employed to determine the porosity of the thin walls.

A Quickvision, PRO system (Mitutoyo, Kawasaki, Kanagawa, Japan) was used to obtain images of the thin walls. The walls were positioned so that the 10 mm × 15 mm surface laid flat on the base of the microscope. A magnification of 2500× and a back-light only setting was used, which resulted in light shining through the pores of porous walls (Fig. 3) and in a black image for dense or quasi-dense walls. Using this back-light only technique also allows the identification of interconnected pores only, which is what is needed for use in electrodes, as the light will only shine through the thin wall if the pores are interconnected, from one side of the wall to the other. Four images were taken at various locations of each wall, in order to get a broader representation of the porosity in the specimen.

Each image was then processed with ImageJ, an open source image processing programme developed by the National Institutes of Health and the Laboratory for

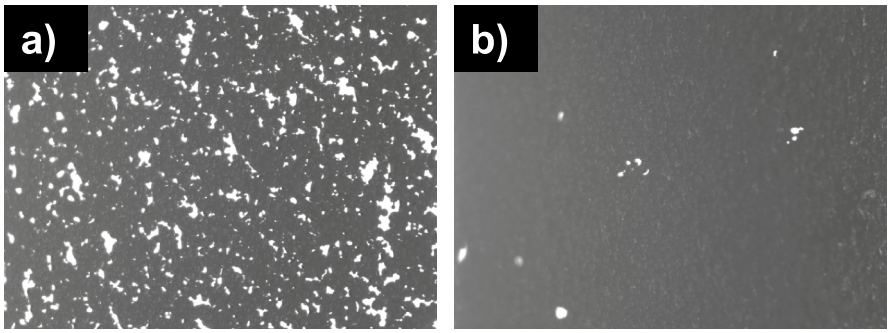

Fig. 3 Illustration of the difference in light between specimens with different levels of porosity when seen with back-light only on the Quickvision, PRO system. **a** BS0 (0/100), duty cycle 50%, power 100 W, scan speed 1500 mm/s; **b** BS0 (0/100), duty cycle 75%, power 100 W, scan speed 1000 mm/s. Showing the difference in image output for specimens with distinct porosity

Optical and Computational Instrumentation (University of Wisconsin, Wisconsin, USA), where the density, as a percentage of the area, was obtained using the maximum entropy threshold. The density of the 4 images per specimen was averaged to obtain the density of the entire specimen. The standard error was calculated based on the standard deviation between the repeats to produce error bars in subsequent graphs.

Finally, a Phenom XL Desktop (Thermo Fisher Scientific Waltham, Massachusetts, USA) Scanning Electron Microscope (SEM) was used to obtain further information about the morphology of particles and the melted state of the thin walls.

Results

The following sections report the diameter of the struts, as well as the thickness and porosity findings for the porous thin walls. These will be compared in terms of beam shape, duty cycle, laser power and scan speed. Comprehensive parameters, such as energy density, resulted in a wide spectrum of results (e.g. for a same energy density, thin wall thickness varied from around 150 to 300 µm) and hence are not a useful parameter to understand the relationships between the process parameters and the resulting thin walls and fine struts.

Fine Struts

Figure 4 shows the diameter of the fine struts with respect to the exposure time for various laser powers and beam shape indexes. It can be observed that for all beam shape indexes, using a laser power of 100 W resulted in the smallest diameter values. For BS0 (0/100) and BS3 (50/50), increasing the laser power increased the diameter of the struts. Similarly, increasing the exposure time resulted in a larger diameter. For example, for BS0 (0/100) and laser power 100 W, there was a 59% difference between the diameter values for an exposure time of 50 µs and

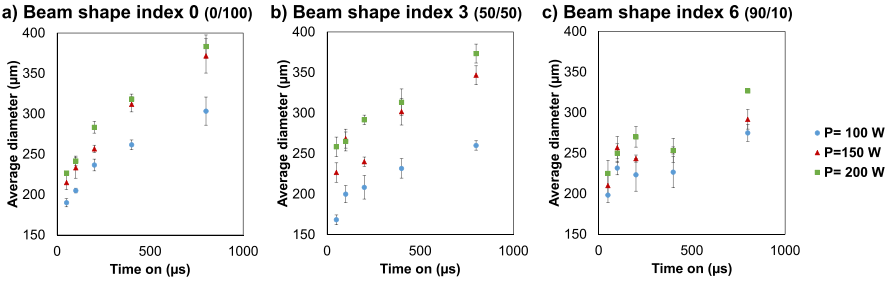

Fig. 4 Graphs of the variation of strut diameter with scan speed and laser power for (**a**) BS0 (0/100); (**b**) BS3 (50/50); (**c**) BS6 (90/10). This clearly illustrates the increase in strut diameter with increasing laser power and exposure time

800 µs. These results are expected, as reducing the power and the exposure time have been previously shown to result in smaller meltpools and thus, smaller strut diameters [13]. The trends of increasing diameter with increasing laser power and exposure time are less obvious for BS6 (90/10), where there were more variations and overlaps between the different powers and exposure times. For example, for BS6 (90/10), an exposure time of 400 µs resulted in an almost identical strut diameters when increasing the laser powers from 150 to 200 W. Another interesting observation is that, for BS6 (90/10), laser powers of 100 and 150 W showed a very small change in strut diameter of 4% and 5%, respectively, when increasing the exposure time from 100 µs to 200 µs, whereas the diameter augmented by 8% for a power of 200 W. Although the differences in diameters are relatively small (< 10%) and that they overlap with the calculated standard error, this still highlights the lack of clear trend for BS6 (90/10), compared to BS0 (0/100) and BS3 (50/50). The smallest strut diameter was 168 ± 6 µm - obtained with BS3 (50/50), 100 W laser power and 50 µs exposure time – whereas the largest measured diameter was 383 ± 14 µm – for BS0 (0/100), 200 W laser power and 800 µs exposure time. These dimensions are in the same range as those reported by Guaglione et al., who produced Zn-0.5Mg lattice structures using SPE, with strut diameters between 130 and 350 µm [24].

As reported above, using a laser power of 100 W resulted in the smallest strut diameters. It is therefore interesting to observe the struts fabricated with a laser power of 100 W, for the various exposure times and beam shape indexes, in Fig. 5. From this figure, the increase in strut diameter with an increasing exposure time can clearly be seen for BS0 (0/100), and slightly less for BS3 (50/50) and BS6 (90/10). Despite some perceived differences in aspect ratio for the different beam shape indexes at a set power and exposure time, it was on average 1 for all of the struts, indicating that the beam shape did not significantly impact the aspect ratio and mainly affected the diameter. Additionally, Fig. 5 visually shows an increase in the number of powder particles fused to the circumference of the strut as the exposure time increases, for all beam shape indexes. This is particularly evident for BS0 (0/100) when comparing 50 µs and 800 µs exposure times.

Figure 6 shows images of the struts with an exposure time of 50 µs – as it is the exposure time with which the smallest strut diameters were produced– for various

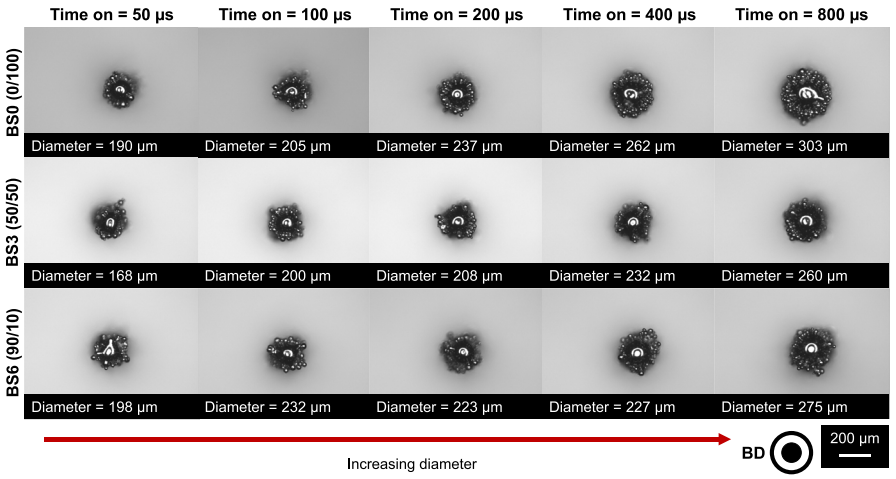

Fig. 5 Images of struts for a laser power of 100 W, with varying exposure times and beam shape indexes. This shows the increase in strut diameter and the number of fused powder particles with an increasing exposure time

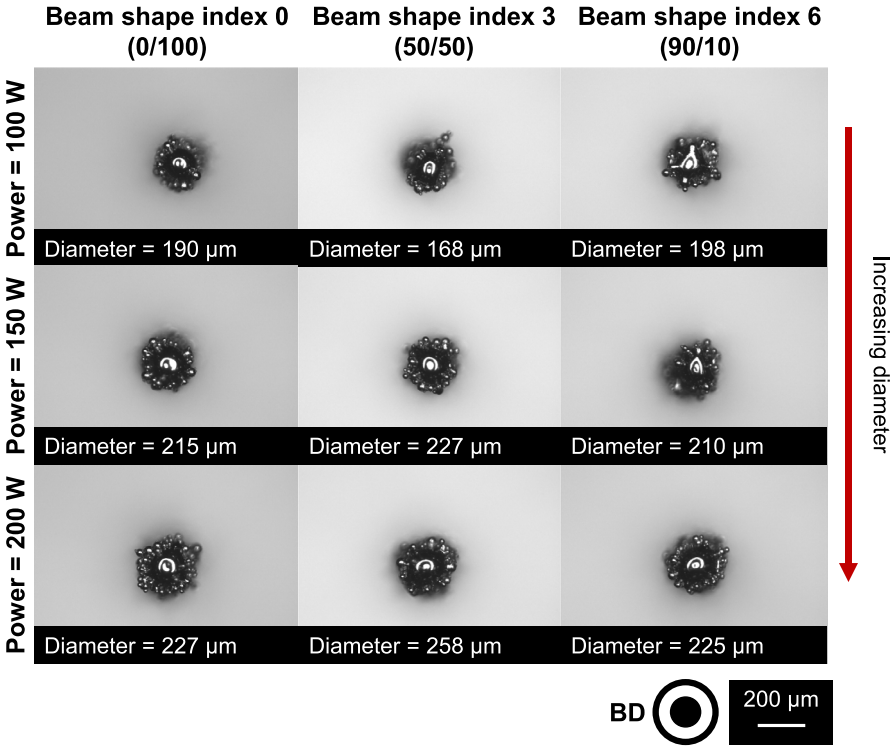

Fig. 6 Images of struts for a time on of 50 µs with varying laser power and beam indexes. This shows the increasing strut diameter with increasing laser power. The effect of using different beam indexes is also visible

laser powers and beam shape indexes. In this figure, the increase in diameter with laser power is clearly visible. An interesting observation from this figure is the effect of the beam shape index on the diameter for a set power and exposure time. Indeed, for laser powers of 150 and 200 W, the strut diameters for BS6 (90/10) were smaller than for BS0 (0/100) and BS3 (50/50) specimens, despite the diameter of BS6 (90/10) being roughly three times bigger than that of BS0 (0/100). In these cases, the diameters of the BS6 (90/10) struts were very close in value to those of BS0 (0/100) (e.g. 2% smaller at a power of 150 W). However, for a laser power of 100 W, using BS3 (50/50) resulted in the smallest strut diameter.

Overall, the results showed that the strut diameters became larger when fabricated with increasing laser power and exposure time. While the beam shape index affected the diameters, the trend is less obvious and will be further investigated in the "Discussion" section.

Porous Thin Walls

In this section, the thickness and porosity of the thin walls are reported separately. It is worth noting that the majority of the thin walls did not reach their final height of 10 mm during this mixed experimental run (see Fig. 7). It is difficult to conclude whether the process parameters or if the interaction between the different specimens during the build caused this. Therefore, this point will not be further investigated in this study.

Wall Thickness

The thinnest wall fabricated had a thickness of 130 µm (obtained with BS0 (0/100), duty cycle 50%, laser power 100 W and 1500 mm/s scan speed), while the largest was 346 µm thick (obtained with BS6 (90/10), duty cycle 100%, power

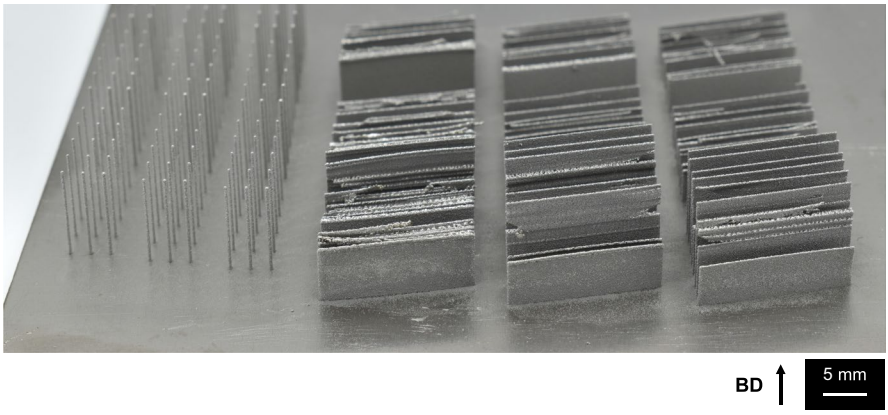

Fig. 7 Photograph of the build plate showing the fine struts and the thin walls. The majority of the thin walls did not reach the final designed height, whereas the fine struts had no such problems

150 W and scan speed 500 mm/s). The average wall thickness, regardless of the parameters employed, was around 207 ± 4 µm thick.

Figure 12 in the Appendix reports the wall thickness measurements with respect to scan speed for all laser powers, duty cycles and beam shape indexes. It was observed that for most specimens, using a laser power of 100 W resulted in thinner tracks than using 150 and 200 W power. However, this was not always the case, as shown in Fig. 8b for BS6 (90/10) and a duty cycle of 100%, where most wall thicknesses were of similar value and in the same range, regardless of laser power. Further, contrary to what was projected, increasing the scan speed, for a set beam shape index and duty cycle, did not necessarily result in a thinner wall (e.g. Fig. 8a for laser powers 150 and 200 W).

For BS0 (0/100) and BS6 (90/10), there is an increase in wall thickness when the duty cycle is increased (Fig. 8a and b, respectively). However, for BS3 (50/50), increasing the duty cycle for a set power and scan speed did not necessarily result in an increase in wall thickness. This was not expected as a duty cycle of 100% is in fact a CW laser, which has been shown to result in larger wall thicknesses, compared to its PW counterpart.

On average, walls fabricated with BS0 (0/100) had a thickness of 196 ± 8 µm, while BS3 (50/50) walls had an average thickness of 202 ± 31 µm and BS6 (90/10) walls were 225 ± 33 µm thick. From this, it seems that increasing the beam shape index increases the thickness of the thin walls. For a duty cycle of 50% and a set laser power and scan speed, increasing the beam shape index resulted in an increase in wall thickness (Fig. 8a). However, for a duty cycle of 75% and 100%, the results are more similar across the different beam shape indexes for a set power and speed. Therefore, increasing the beam shape index does not result in a clear trend with respect to the wall thickness.

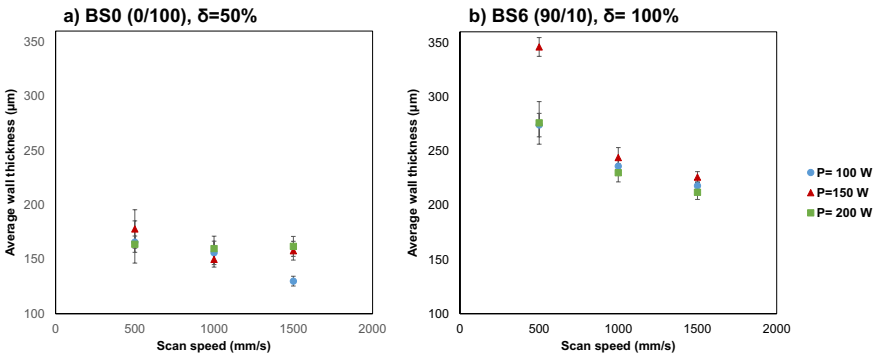

Fig. 8 Graphs showing the variation of wall thickness with respect to scan speed for various laser powers. (**a**) δ = 50%, BS0 (0/100); (**b**) δ = 100%, BS6 (90/10). Increasing the beam shape index, laser power and duty cycle generally resulted in thicker walls while some disparities were also observed

Porosity

Figure 13, in the Appendix, reports the porosity of all of the thin walls with respect to scan speed for the various laser power, duty cycle and beam shape index investigated. As previously mentioned, porosity was only measured for specimens through which light could pass (Fig. 3). Other specimens were assumed to be near-fully dense. Therefore, only 40 specimens (out of 81) for which porosity was detected are shown in Fig. 13. Using a duty cycle of 50% resulted in the highest amount of porous walls, with 20 specimens, compared to duty cycles of 75% and 100%, with 12 and 8 porous specimens, respectively.

In terms of beam shape index, BS0 (0/100) had the smallest amount of porous walls (10 specimens), compared to BS3 (50/50) and BS6 (90/10) (which had 13 and 17 porous walls, respectively), particularly at higher duty cycles. However, despite having the smallest number of porous walls, BS0 (0/100) specimens had, on average, higher porosity levels than BS3 (50/50) and BS6 (90/10)by 8% and 51%, respectively.

As one could assume, specimens fabricated with high scan speeds (e.g. 1500 mm/s) had higher porosity than specimens made with lower speeds (500 mm/s or 1000 mm/s). Similarly, using a laser power of 100 W resulted in 20 porous specimens for various beam shape indexes and duty cycles, as well as having the highest porosity among the other specimens. Indeed, the most porous thin wall was obtained with BS0 (0/100), duty cycle 50%, laser power 100 W and scan speed 1500 mm/s and had a porosity of $19.43 \pm 0.5\%$.

An assumption could be that the thinner walls resulted in higher porosity, due to the low energy inputs required to fabricate these. However, no clear trend emerged between the porosity level and the wall thickness for various beam shapes. This indicates that the porosity present is not necessarily linked to the wall thickness. This figure also clearly shows the smaller wall thicknesses obtained for BS0 (0/100).

Figure 9 presents SEM images of the thin walls for various beam shape indexes and duty cycles. From this figure, it is clear that using a duty cycle of 50% resulted in the presence of more pores for all beam shape indexes. All thin walls presented different amounts of pores and melted areas. For example, Fig. 9a shows pores of various sizes as well as consolidated "melted areas". As the duty cycle increases for a set beam shape index, more powder particles are fully melted and the porosity observed is in the form of irregular pores or lack of fusion defects rather than circular pores (e.g. Fig. 9d). In some thin walls, some particles were partially, rather than fully, melted (e.g. Fig. 9c, i). For specimens manufactured with BS6 (90/10), there was a large number of sintered powder particles on the surface of the thin wall (Fig. 9f), when compared to BS0 (0/100) (Fig. 9d) and BS3 (50/50) (Fig. 9e). The melted areas in Fig. 9e are interesting as it is possible to observe a "stacking" or overlap of these, which have not adequately fused together.

Figure 10 presents SEM images of thin walls for various scan speeds (for a set beam shape index, laser power and duty cycle). All images show both pores and melted areas and the amount of porosity increases as the scan speed increases. Figure 10a has a higher quantity of melted areas and few sintered powder particles on the surface of the wall, compared to the other scan speeds. This is attributed

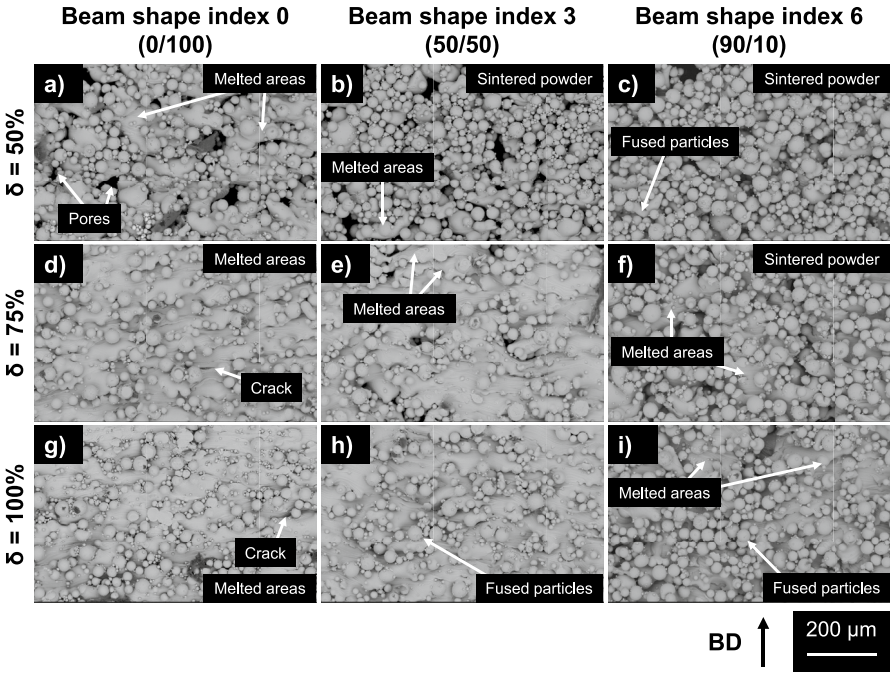

Fig. 9 SEM images of the porosity and melted areas present in the thin walls, which were built with a laser power of 100 W and scan speed of 1000 mm/s with (**a**) δ = 50% and BS0 (0/100); (**b**) δ = 50% and BS3 (50/50); (**c**) δ = 50% and BS6 (90/10); (**d**) δ = 75% and BS0 (0/100); (**e**) δ = 75% and BS3 (50/50); (**f**) δ = 75% and BS6 (90/10); (**g**) δ = 100% and BS0 (0/100); (**h**) δ = 100% and BS3 (50/50); (**i**) δ = 100% and BS6 (90/10). This shows the higher number of pores present for a duty cycle of 50% and the higher number of sintered powder particles on the thin walls for BS6 (90/10) specimens

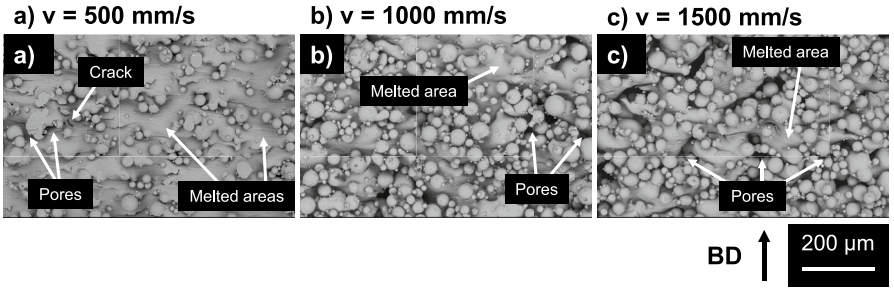

Fig. 10 SEM images of the porosity of thin walls manufactured with BS3 (50/50), δ = 50% and a laser power of 150 W with (**a**) scan speed = 500 mm/s; (**b**) scan speed = 1000 mm/s; (**c**) 1500 mm/s. This shows the increase in porosity as the scan speed increase

to a higher energy input, from the lower scan speed utilised, which resulted in partial melting of particles adjacent to the surfaces of the thin wall. However, as well as circular pores, irregular ones are also present in the specimen. Specimens manufactured with a scan speed of 500 mm/s had, on average, pores of 14.5 µm

diameter, while scan speeds of 1000 mm/s and 1500 mm/s had pore diameters of 23.5 and 31 µm respectively. It can hence be surmised that larger pores are formed at higher scan speeds. An interesting observation in Fig. 10c is the somewhat regular spacing of the pores present, which may be linked to the use of a duty cycle of 50%.

Figure 11 shows the effect of laser power on the porosity of the thin walls. From this figure, it can be seen that at a power of 100 W, there are numerous powder particles on the surface of the thin wall (Fig. 11a), as the power was probably not high enough to melt the particles together. This also resulted in the presence of pores. It is clear from this figure that a laser power of 200 W resulted in the highest amount of melted areas (Fig. 11c) and the least porosity.

Overall, this "Results" section showed that the various process parameters had an effect on the diameter of the struts, as well as the thickness and porosity of the thin walls. As expected, high scan speeds, low laser powers, and low exposure times, where applicable, resulted in smaller strut diameters and wall thicknesses, as well as higher porosity. More interestingly, the duty cycle and beam shape index affected the parts as well. The duty cycle had a clear effect on the porosity of thin walls where the duty cycle of 50% produced the highest number of porous walls and had the highest porosity. However, for the wall thicknesses, an increase was observed when the duty cycle was augmented, however, this was only the case for beam shape indexes of 0 and 6. This trend was not observed for BS3 (50/50). This shows the importance of the beam shape index, where there were less obvious trends. For example, the strut diameters did not vary as expected with increasing power and exposure time for BS6 (90/10). Similarly for the wall thickness, increasing the beam shape index seems to increase the wall thickness for a duty cycle of 50%, but that is not the case for higher duty cycles, putting the initial trend into question.

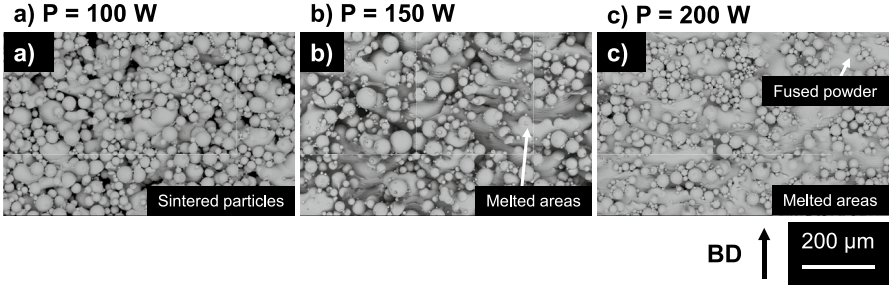

Fig. 11 SEM image of the thin walls for BS3 (50/50), δ = 50%, scan speed 1000 mm/s and (**a**) power = 100 W; (**b**) power = 150 W; (**c**) power = 200 W. This shows that an increasing laser power produces more melted areas and less porosity is present

Discussion

As the effect of laser power, scan speed and exposure time have been previously investigated and are generally understood, this "Discussion" section will focus on duty cycle and beam shape index and their effects when producing fine and porous structures.

Effect of Temporal Laser Control on Porous Thin Walls

The "Results" section showed that using a duty cycle of 50% resulted in the thinnest walls, as well the most porous walls. Indeed, the thinnest wall (with a thickness of 130 µm) was obtained for BS0 (0/100), duty cycle 50%, laser power 100 W and 1500 mm/s scan speed. On the other hand, the thickest wall was fabricated with a duty cycle of 100%. These results seem to show that increasing the duty cycle results in thicker tracks. This observation can be explained as a higher duty cycle is linked to a higher exposure time of the laser on the powder bed, which leads to larger meltpools, and hence, thicker tracks. Indeed, Hojjatzadeh et al. found that when the duty cycle decreased, the meltpool size decreased as well for Al6061 [25]. Further, Vasileska et al. clearly visualised the effect of the duty cycle on meltpool size of AISI 316 L and surmised that the duty cycle can be used to control the energy density [26]. Laag et al. also concluded that a duty cycle of 100% resulted in excessive melting and meltpool enlargement for Inconel 718 [27]. However, the increase in wall thickness with an increase in duty cycle was only the case for BS0 (0/100) and BS6 (90/10) increased (see Fig. 12a, d, g and c, f, i, respectively), and not for BS3 (50/50). The reasoning for this is given in the following sub-section.

Regarding the porosity of the thin walls, Fig. 13 showed that using a duty cycle of 50% resulted in a higher number of porous specimens, while Fig. 9 showed that specimens fabricated with a duty cycle of 50% had more pore formation than higher duty cycles. This can be explained by the PW laser characteristics: at a lower duty cycle, the laser on time is less than at higher duty cycles. Thus, there is less time for particles to melt together into one solid part, hence increasing the likelihood of obtaining higher porosity in the specimens. Similarly, Hojjatzadeh et al. found that cavities and pores formed in meltpools because of the rapid solidification caused by PW laser [25]. Overall, duty cycle is a key parameter to obtain porous thin walls. Utilising a low duty cycle has been shown to result in thinner tracks and higher porosity due to the reduced interaction of the laser, regardless of the power and shape, with the powder bed. From these results, it can be surmised that the main porosity mechanism in the thin walls, as a result of the duty cycle, was lack-of-fusion rather than keyhole formation. Indeed, for lower duty cycles, more porosity was observed, and the longer cooling period is more likely to result in under melting, and hence lack-of fusion.

In summary, the duty cycle is effective in controlling the energy density of meltpools, which can impact both the feature resolution, as well as the porosity present in fine structures.

Effect of Spatial Beam Shaping on Fine Structures

The results showed that the thinnest wall obtained using BS0 (0/100) was 130 µm, while the thinnest walls fabricated with BS3 (50/50) and BS6 (90/10) were 152 and 184 µm, respectively. This result is logical as the beam diameter of BS0 (0/100) was 49 µm, the smallest compared to BS3 (50/50) and BS6 (90/10), which had a beam diameter of 112 and 144 µm, respectively. Despite this, the thinnest track for BS0 (0/100) was 2.7 times larger than its beam diameter. For BS3 (50/50) and BS6 (90/10), the smallest wall thicknesses were 1.4 and 1.3 times larger than their beam diameters, respectively. From these values, BS0 (0/100) seems to result in the largest meltpools, relative to its beam diameter, while BS6 (90/10) has the smallest. It can be incurred that using BS0 (0/100) results in a higher intensity due to the Gaussian shape of the beam. BS6 (90/10), on the other hand, has a ring shape which distributes the energy input in a wider area and hence reduces the maximum intensity to result in smaller meltpool formation, relative to its beam diameter. This analysis seems in line with other studies which have shown that beam shaping directly influences the meltpool characteristics both for Stainless steel 316 L [28] and for aluminium alloys [29]. Indeed, Ayoola et al. found that the spatial energy distribution of the beam had a significant influence on the geometry of S275 mild steel weld beads due to the change in energy density [30]. Similarly, Galbusera et al. found that the beam intensity profile affected the LPBF meltpool's temperature distribution and that using a ring shaped beam resulted in a more homogeneous temperature distribution and larger meltpool width for the same volumetric energy density, for aluminium alloys [19]. Therefore, although a higher beam shape index (e.g. BS6 (90/10)) results in a wider meltpool, the better distribution of energy density means that, relative to the beam diameter, the meltpool size is smaller than for a lower beam shape index (e.g. BS0 (0/100)). The localised concentration of the energy input for the various beam shape indexes could also explain why the smallest strut diameter (168 ± 6 µm) was obtained for BS3 (50/50), and not BS0 (0/100), despite the difference in beam size. Indeed, BS3 (50/50) may present itself as a good compromise between a small beam diameter and a more homogeneous temperature distribution.

Furthermore, thin walls manufactured with BS6 (90/10), had a larger number of sintered powder particles on the surface (e.g. Fig. 9f) than BS0 (0/100) (Fig. 9d) and BS3 (50/50) walls (e.g. Fig. 9e). This could also be linked to the more homogeneous power density distribution, which caused the powder to not fully melt on the surface. This is in line with the findings of Okunkova et al., who showed that using a non-Gaussian laser power density distribution decreased the powder-free zones around single-tracks, due to the decrease in width of the thermal influence area [31].

Another interesting result was that BS0 (0/100) had the smallest number of porous thin walls but these had some of the highest levels of porosity, notably 51% more porous than specimens made with BS6 (90/10), which had the highest number of porous specimens. The localised concentration of energy input might also explain the results obtained for the number of porous walls. The BS6 (90/10) thin walls showed a higher number of sintered particles (Fig. 9f) rather than melting, thus creating a porous thin wall due to the less localised concentration of energy. Galbusera et al. also found that the decrease in power in the central part

of the beam for BS6 (90/10) means that it would require higher laser power to ensure full densification [19]. Further, Roehling et al. determined that a ring beam shape resulted in a shallower meltpool, for a set power energy density, which may lead to lack of fusion defects [32]. On the contrary, BS0 (0/100) specimens had more concentrated energy inputs which resulted in more melting of the powder particles and hence, a lesser number of porous specimens. The higher porosity level present in BS0 (0/100) specimens may also be due to the high localised power input, which is well known to result in porosity and defects, such as the formation of keyhole porosity. This was also observed by Galbusera et al. who explained that the morphology of the Gaussian beam resulted in a deeper penetration of the material which may push the process in the keyhole regime [19] with a pulsating keyhole [33] and spherical pores caused by gas entrapment [34].

The penetration depth of the laser and the adherence to the previous layer are also affected by the beam shape index, where BS6 (90/10) may have lower penetration depth due to the higher energy profile at the edges instead of in the centre [19]. This may explain the overlapping "layers", observed in Fig. 9e for BS3 (50/50), which do not seem to be fully adhered to the previous layer. A "fish-scale" morphology of the track was also observed by Jun et al. when using PW [35].

Additionally, using a ring shaped beam profile can be particularly useful to enlarge the processing window for LPBF. Indeed, Cloots et al. found that using a ring profile reduced hot cracking [36], while Wischeropp et al. observed fewer defects, protrusions and porosity for a higher beam shape index in AlSi10Mg [37], thus resulting in a larger, more robust and more stable [38] process window. This higher stability also means that using ring beam shape profiles can increase the productivity of LPBF, as shown by Grünewald et al., for AISI 316 L [39]. This may explain why when manufacturing the fine struts in this study, increasing the laser power for BS0 (0/100) and BS3 (50/50) resulted in an increase in strut diameter, whereas this was not the case for BS6 (90/10) where a lack of trend was observed. This was also the case for the thin walls, where for a duty cycle of 100%, the wall thicknesses of BS6 (90/10) specimens were of similar values, regardless of laser power.

In summary, the various beam shape indexes resulted in a different beam diameter and a different energy input localisation, which in turn affected the temperature distribution in the meltpool and hence, the meltpool characteristics. These are responsible for the differences in wall thickness and porosity, as well as the diameter of the fine struts. It is important to note that beam shaping did not create thinner walls than is currently possible with conventional LPBF lasers. However, BS3 (50/50) and BS6 (90/10) produced thin specimens relative to their beam diameter, due to the more homogenous temperature distribution. Therefore, reducing the beam diameter of BS3 (50/50) and BS6 (90/10) in the future could lead to the fabrication of thinner walls than is currently possible. Further, the beam shape indexes had a significant effect on porosity, whereby varying the beam shape index changed the pore formation mechanism from keyhole with BS0 (0/100) to lack-of-fusion with BS6 (90/10). Therefore, beam shaping offers more control over meltpool dynamics, which in turn affects the feature resolution and porosity of the part.

Overall, this "Discussion" section showed that temporal and spatial control of the beam are key to controlling the deposition mechanisms in LPBF. Therefore, by adequately choosing and controlling the duty cycle and spatial distribution of the emission power, the feature resolution, porosity and microstructure of LPBF can be tailored. In order to obtain fine and porous structures, it is therefore recommended to select a low duty cycle (e.g. 50% or less) as well as a mixed beam profile composed of a central peak and a ring, such as BS3 (50/50), which may give a good compromise between inherent beam diameter and stable processing conditions.

Conclusions

The aim of this study was to utilise beam shaping, PW, SPE and other LPBF process parameters to produce Ti-6Al-4V porous thin walls and fine struts to facilitate the manufacturing of gas diffusion layers of regenerative fuel cells for renewable energy applications. To do this, PW, SPE were utilised and the duty cycle, beam shape index, laser power and scan speed were varied to manufacture thin porous walls and fine struts. Some of the key findings from this study include:

- The thinnest wall was 130 µm wide (BS0 (0/100), duty cycle 50%, laser power 100 W and 1500 mm/s scan speed) while the smallest strut had a diameter of 168 µm (BS3 (50/50), 100 W laser power and 50 µs exposure time).
- As expected, high scan speeds and low laser powers (as well as low exposure times, where applicable,) resulted in smaller strut diameters and wall thicknesses, as well as higher porosity.
- The duty cycle had a clear effect on the porosity of thin walls, where the duty cycle of 50% produced the highest number of porous walls and had the highest porosity.
- The thin wall thickness was affected by a strong interaction between the duty cycle and the spatial distribution of the laser emission power. BS6 (90/10) is expected to result in a more homogeneous temperature distribution which produced specimens with a higher porosity.
- Recommendation to obtain fine and porous structures: selecting a low duty cycle (e.g. 50% or less) as well as redistributing the emission power from the inner core of the fiber towards the outer ring (i.e. BS3 (50/50) or BS6 (90/10)), provide stable processing conditions.

Overall, this study showed that temporal and spatial control of the beam (through duty cycle and beam shape index) are powerful tools for manipulating the deposition mechanisms in LPBF. Therefore, by adequately choosing and controlling the duty cycle and spatial distribution of the laser power, the feature resolution, porosity and microstructure of LPBF-deposited materials can be controlled. Future work could include further investigation of the trade-off between the different irradiance profiles

and feature resolution, investigating the underlying physics and effects of different beam shapes on the microstructure and mechanical properties of specimens, as well as testing electrochemically the LPBF-manufactured thin porous structures. To conclude, this study demonstrates the capabilities of temporal laser control and spatial beam shaping to fabricate parts with tailor-made feature resolution, porosity and microstructures for energy applications.

Appendix

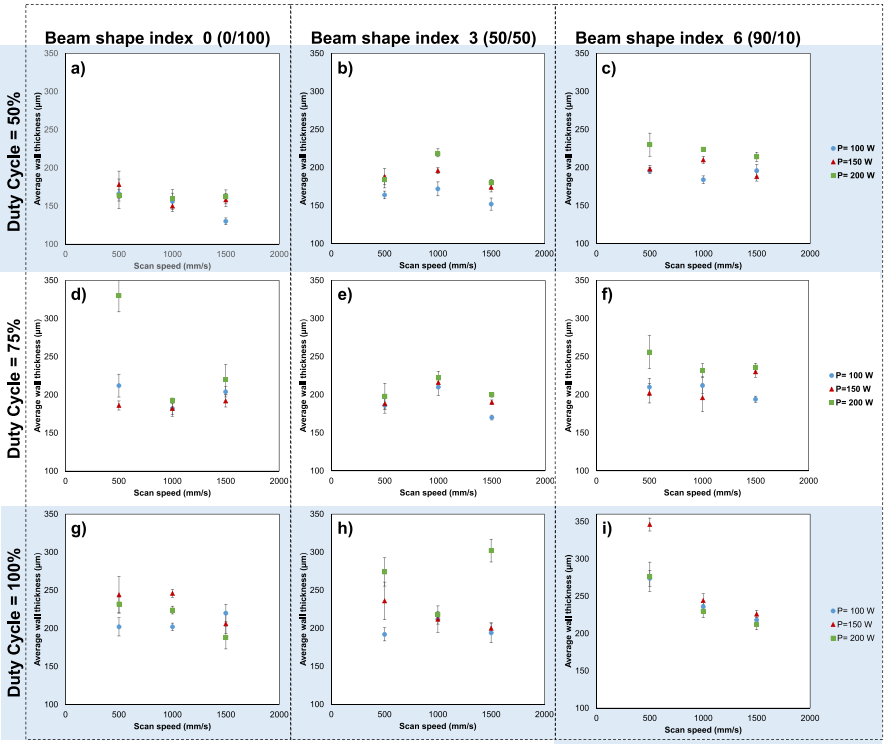

Fig. 12 Graphs showing the variation of wall thickness with respect to scan speed for various laser power, duty cycles and beam shape indexes. (**a**) δ = 50%, BS0 (0/100); (**b**) δ = 50%, BS3 (50/50); (**c**) δ = 50%, BS6 (90/10); (**d**) δ = 75%, BS0 (0/100); (**e**) δ = 75%, BS3 (50/50); (**f**) δ = 75%, BS6 (90/10); (**g**) δ = 100%, BS0 (0/100); (**h**) δ = 100%, BS3 (50/50); (**i**) δ = 100%, BS6 (90/10). This graph shows the lack of clear trends regarding the effect of laser power, scan speed, duty cycle and beam shape index

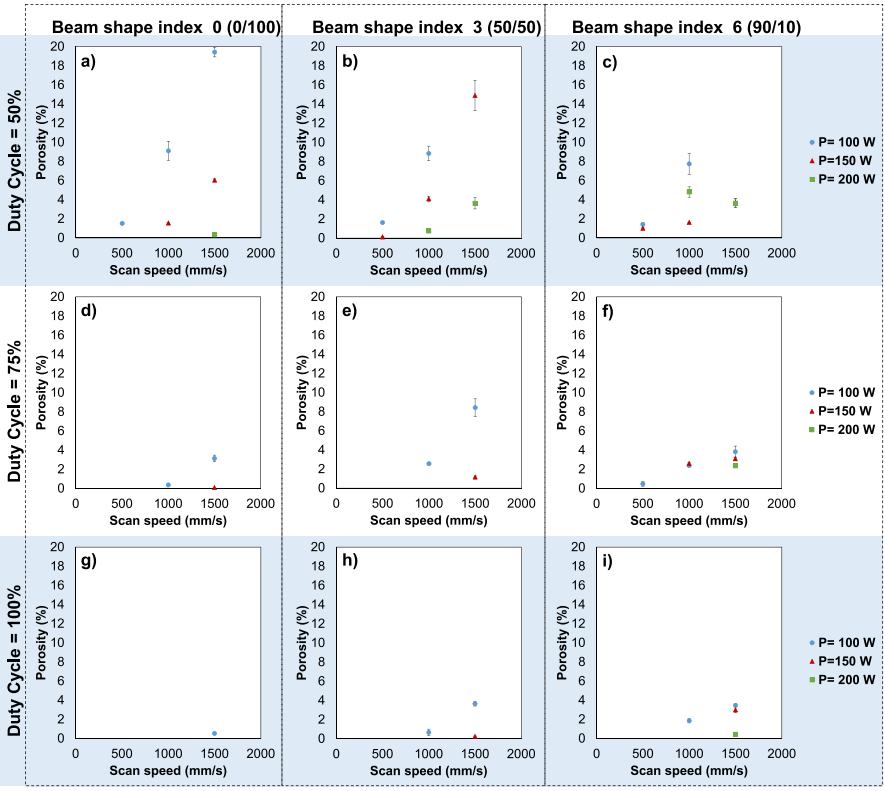

Fig. 13 Graphs showing the variation of porosity with respect to scan speed for various laser power, duty cycles and beam shape indexes. (**a**) δ = 50%, BS0 (0/100); (**b**) δ = 50%, BS3 (50/50); (**c**) δ = 50%, BS6 (90/10); (**d**) δ = 75%, BS0 (0/100); (**e**) δ = 75%, BS3 (50/50); (**f**) δ = 75%, BS6 (90/10); (**g**) δ = 100%, BS0 (0/100); (**h**) δ = 100%, BS3 (50/50); (**i**) δ = 100%, BS6 (90/10). This shows the higher number of porous specimens fabricated with a duty cycle of 50% and with BS6 (90/10). Further, increasing the laser power resulted in less porous specimens whereas increasing the scan speed resulted in higher levels of porosity

Acknowledgements This research was carried out under project number 4000135470/21/NL/GLC/ov, which is a part of the Discovery (Early Technology Development) program of the European Space Agency. The views expressed herein can in no way be taken to reflect the official opinion of the European Space Agency and are not intended to endorse particular technologies, companies, or products. The Italian Ministry of Education, University and Research (MIUR) is acknowledged for the support provided through the National Plan for Recovery and Resilience (PNRR). The authors are grateful to Optoprim Srl for the longstanding collaboration and to nLIGHT for the technical assistance. Raylase is acknowledged for the support provided to the LPBF system. Thanks are given to Francesco Galbusera for his help and advice in operating the LPBF system at the Politecnico di Milano. The authors would also like to acknowledge 4TU.HTM funding for Joint Materials Science Activities and the University of Twente MS3 Microscopy Lab.

Author Contributions

- Salomé Sanchez: Conceptualisation, Methodology, Data Curation, Formal Analysis, Investigation, Validation, Visualisation, Writing-original draft, Writing-review & editing
- Ahmad Zafari: Writing-review & editing

• Leonardo Caprio: Supervision, Methodology, Writing-review & editing
• Ali Gokhan Demir: Project administration, Resources, Supervision, Methodology, Writing-review & editing
• Davoud Jafari: Funding Acquisition, Project administration, Conceptualisation, Supervision, Writing-review & editing.

Funding This research was carried out under project number 4000135470/21/NL/GLC/ov, which is a part of the Discovery (Early Technology Development) program of the European Space Agency. The authors would also like to acknowledge 4TU.HTM funding for Joint Materials Science Activities. The Italian Ministry of Education, University and Research (MIUR) is acknowledged for the support provided through the National Plan for Recovery and Resilience (PNRR).

Data Availability The datasets generated during and/or analysed during the current study are available from the corresponding author on reasonable request.

Declarations

Ethical Approval Not applicable.

Competing Interests The authors declare no competing interests.

References

1. Choi, H., Kim, O.H., Kim, M., Choe, H., Cho, Y.H., Sung, Y.E.: Next-generation polymer-electrolyte-membrane fuel cells using titanium foam as gas diffusion layer. ACS Appl. Mater. Interfaces. **6**(10) (2014). https://doi.org/10.1021/am500962h
2. Doan, T.L., et al.: A review of the porous transport layer in polymer electrolyte membrane water electrolysis. Int J Energy Res **45**(10), 14207 (2021). https://doi.org/10.1002/er.6739
3. Wang, Y., Leung, D.Y.C., Xuan, J., Wang, H.: A review on unitized regenerative fuel cell technologies, part-A: Unitized regenerative proton exchange membrane fuel cells. Renew Sustain Energy Rev **65**, 961 (2016). https://doi.org/10.1016/j.rser.2016.07.046
4. Yap, C.Y., et al.: Review of selective laser melting: materials and applications. Appl. Phys. Rev. **2**(4) (2015). https://doi.org/10.1063/1.4935926
5. Shipley, H., et al.: Optimisation of process parameters to address fundamental challenges during selective laser melting of Ti-6Al-4V: A review. Int J Mach Tools Manuf **128**, 1–20 (2018). https://doi.org/10.1016/J.IJMACHTOOLS.2018.01.003
6. Gordon, J.V., et al.: Defect structure process maps for laser powder bed fusion additive manufacturing. Addit Manuf **36**, 101552 (2020). https://doi.org/10.1016/J.ADDMA.2020.101552
7. Mishurova, T., Artzt, K., Haubrich, J., Requena, G., Bruno, G.: New aspects about the search for the most relevant parameters optimizing SLM materials. Addit Manuf **25**, 325–334 (2019). https://doi.org/10.1016/J.ADDMA.2018.11.023
8. du Plessis, A., Razavi, S.M.J., Berto, F.: The effects of microporosity in struts of gyroid lattice structures produced by laser powder bed fusion. Mater Des **194**, 108899 (2020). https://doi.org/10.1016/J.MATDES.2020.108899

9. Abele, E., Stoffregen, H.A., Kniepkamp, M., Lang, S., Hampe, M.: Selective laser melting for manufacturing of thin-walled porous elements. J Mater Process Technol **215**(1), 114 (2015). https://doi.org/10.1016/j.jmatprotec.2014.07.017
10. Yadroitsev, I., Shishkovsky, I., Bertrand, P., Smurov, I.: Manufacturing of fine-structured 3D porous filter elements by selective laser melting. Appl Surf Sci **255**(10), 5523–5527 (2009). https://doi.org/10.1016/J.APSUSC.2008.07.154
11. Su, X., Yang, Y., Xiao, D., Luo, Z.: An investigation into direct fabrication of fine-structured components by selective laser melting. Int J Adv Manuf Technol **64**, 9–12 (2013). https://doi.org/10.1007/s00170-012-4081-8
12. Xie, D., Dittmeyer, R.: Correlations of laser scanning parameters and porous structure properties of permeable materials made by laser-beam powder-bed fusion. Addit Manuf **47**, 102261 (2021). https://doi.org/10.1016/J.ADDMA.2021.102261
13. Demir, A.G., Colombo, P., Previtali, B.: From pulsed to continuous wave emission in SLM with contemporary fiber laser sources: Effect of temporal and spatial pulse overlap in part quality. Int J Adv Manuf Technol **91**, 5–8 (2017). https://doi.org/10.1007/s00170-016-9948-7
14. Finazzi, V., Demir, A.G., Biffi, C.A., Migliavacca, F., Petrini, L., Previtali, B.: Design and functional testing of a novel balloon-expandable cardiovascular stent in CoCr alloy produced by selective laser melting. J Manuf Process **55**, 161 (2020). https://doi.org/10.1016/j.jmapro.2020.03.060
15. Jafari, D., et al.: Pulsed mode selective laser melting of porous structures: Structural and thermophysical characterization. Addit Manuf **35**, 101263 (2020). https://doi.org/10.1016/j.addma.2020.101263
16. Finazzi, V., Berti, F., Petrini, L., Previtali, B., Demir, A.G.: Additive manufacturing and post-processing of superelastic NiTi micro struts as building blocks for cardiovascular stents. Addit Manuf **70**, 103561 (2023). https://doi.org/10.1016/J.ADDMA.2023.103561
17. Ghouse, S., Babu, S., Van Arkel, R.J., Nai, K., Hooper, P.A., Jeffers, J.R.T.: The influence of laser parameters and scanning strategies on the mechanical properties of a stochastic porous material. Mater Des **131**, 498–508 (2017). https://doi.org/10.1016/J.MATDES.2017.06.041
18. Grünewald, J., Blickle, V., Allenberg-Rabe, M., Wagenblast, P., Wudy, K.: Flexible and highly dynamic beam shaping for Laser-Based Powder Bed Fusion of metals. Procedia CIRP (2022). https://doi.org/10.1016/j.procir.2022.08.124
19. Galbusera, F., Caprio, L., Previtali, B., Demir, A.G.: The influence of novel beam shapes on melt pool shape and mechanical properties of LPBF produced Al-alloy. J Manuf Process **85**, 1024 (2023). https://doi.org/10.1016/j.jmapro.2022.12.007
20. Zou, X., et al.: Surface structuring via additive manufacturing to improve the performance of metal and polymer joints. Metals (Basel) **11**(4), (2021). https://doi.org/10.3390/met11040567
21. ASTM B822–17.: Standard test method for particle size distribution of metal powders and related compounds by light scattering. ASTM International (2017)
22. Steen, W.M., Mazumder, J.: Laser material processing: 4th edn. (2010). https://doi.org/10.1007/978-1-84996-062-5
23. Caprio, L., Demir, A.G., Previtali, B.: Comparative study between CW and PW emissions in selective laser melting. J. Laser Appl. **30**(3) (2018). https://doi.org/10.2351/1.5040631
24. Guaglione, F., Caprio, L., Previtali, B., Demir, A.G.: Single point exposure LPBF for the production of biodegradable Zn-alloy lattice structures. Addit Manuf **48**, 102426 (2021). https://doi.org/10.1016/J.ADDMA.2021.102426
25. Hojjatzadeh, S.M.H., et al.: In-situ characterization of pore formation dynamics in pulsed wave laser powder bed fusion. Materials **14**(11), 2936 (2021). https://doi.org/10.3390/ma14112936
26. Vasileska, E., Demir, A.G., Colosimo, B.M., Previtali, B.: A novel paradigm for feedback control in LPBF: Layer-wise correction for overhang structures. Adv. Manuf. **10**(2) (2022). https://doi.org/10.1007/s40436-021-00379-6
27. Laag, T., Winkel, T.M., Jauer, L., Heußen, D., Haefner, C.L.: Improvement of part accuracy by combination of Pulsed Wave (PW) and Continuous Wave (CW) laser powder bed fusion. BHM Berg- Huettenmaenn Monatsh **167**(7), 308 (2022). https://doi.org/10.1007/s00501-022-01235-1
28. Matthews, M.J., et al.: Controlling melt pool shape, microstructure and residual stress in additively manufactured metals using modified laser beam profiles. Procedia CIRP (2020). https://doi.org/10.1016/j.procir.2020.09.038
29. Han, J., Shi, Y., Zhang, G., Volodymyr, K., yun Le, W.: Minimizing defects and controlling the morphology of laser welded aluminum alloys using power modulation-based laser beam oscillation. J. Manuf. Process. **83** (2022). https://doi.org/10.1016/j.jmapro.2022.08.031

30. Ayoola, W.A., Suder, W.J., Williams, S.W.: Effect of beam shape and spatial energy distribution on weld bead geometry in conduction welding. Opt Laser Technol **117**, 280 (2019). https://doi.org/10.1016/j.optlastec.2019.04.025
31. Okunkova, A.A., Peretyagin, P.Y., Podrabinnik, P.A., Zhirnov, I.V., Gusarov, A.V.: Development of laser beam modulation assets for the process productivity improvement of selective laser melting. Procedia IUTAM (2017). https://doi.org/10.1016/j.piutam.2017.06.019
32. Roehling, T.T., et al.: Controlling grain nucleation and morphology by laser beam shaping in metal additive manufacturing. Mater Des **195**, 109071 (2020). https://doi.org/10.1016/j.matdes.2020.109071
33. Caprio, L., Demir, A.G., Previtali, B.: Observing molten pool surface oscillations during keyhole processing in laser powder bed fusion as a novel method to estimate the penetration depth. Addit Manuf **36**, 101470 (2020). https://doi.org/10.1016/j.addma.2020.101470
34. Zhao, C., et al.: Critical instability at moving keyhole tip generates porosity in laser melting. Science **370**(6520), 2020 (1979). https://doi.org/10.1126/science.abd1587
35. Song, J., Tang, Q., Setchi, R., Ryan, M.: A comparative study of pulse wave and continuous wave laser patterns during laser powder bed fusion. In: Smart innovation. Syst Technol (2023). https://doi.org/10.1007/978-981-19-9205-6_27
36. Cloots, M., Uggowitzer, P.J., Wegener, K.: Investigations on the microstructure and crack formation of IN738LC samples processed by selective laser melting using Gaussian and doughnut profiles. Mater Des **89**, 770 (2016). https://doi.org/10.1016/j.matdes.2015.10.027
37. Wischeropp, T.M., Tarhini, H., Emmelmann, C.: Influence of laser beam profile on the selective laser melting process of AlSi10Mg. J Laser Appl **32**(2), 022059 (2020). https://doi.org/10.2351/7.0000100
38. Zhirnov, I.V., Podrabinnik, P.A., Okunkova, A.A., Gusarov, A.V.: Laser beam profiling: Experimental study of its influence on single-track formation by selective laser melting. Mech. Ind. **16**(7) (2015). https://doi.org/10.1051/meca/2015082
39. Grünewald, J., Gehringer, F., Schmöller, M., Wudy, K.: Influence of ring-shaped beam profiles on process stability and productivity in laser-based powder bed fusion of AISI 316L. Metals (Basel). **11**(12), (2021). https://doi.org/10.3390/met11121989

Authors and Affiliations

Salomé Sanchez[1] · Ahmad Zafari[1] · Leonardo Caprio[2] · Ali Gökhan Demir[2] · Davoud Jafari[1]

[1] Department of Design Production and Management, Faculty of Engineering Technology, University of Twente, Enschede, Netherlands

[2] Department of Mechanical Engineering, Politecnico di Milano, Via La Masa 1, Milan 20156, Italy